Atomic structure and energetics of amorphous-crystalline CuZr interfaces: A molecular dynamics study

X.Z. Gao[1], **M. H. Müser**[2], **L. T. Kong**[1]‡, **J. F. Li**[1]

[1] State Key Laboratory of Metal Matrix Composites, School of Materials Science and Engineering, Shanghai Jiao Tong University, 800 Dongchuan Road, Minhang, Shanghai 200240, CHINA.

[2] Jülich Supercomputing Centre (JSC), Wilhelm-Johnen-Strasse, 52425 Jülich, Germany & Department of Materials Science and Engineering, Universität des Saarlandes, Saarbrücken, Germany.

Abstract. The local order of the binary alloy CuZr differs between the crystal (B2 phase) and the metallic glass (MG). In the B2 phase, both Cu and Zr reside in the center of polyhedra whose surfaces are composed of six tetragons and eight hexagons. In the glass, many different polyhedra occur with a large fraction of five-edged faces. However, little has been known hitherto about the local order in the interfacial region between glass and crystal. Using embedded-atom potential based molecular-dynamics simulations, we find it differs markedly from that in the glass. For example, distinctly fewer pentagons occur on the surfaces of Voronoi polyhedra in the interface than on those in the MG. Moreover, there is an increased variety of polyhedra allowing the interface to be more densely packed than the MG. Details of the polyhedra distribution and consequently various interfacial properties depend on the orientation of the crystals and to some degree also on the thermal history of the sample. For the investigated surfaces we find that the interfacial energy is the smallest and the crystallization activation energy highest for the closest-packed crystalline surface. This result can be rationalized by the argument that the lattice spacing of the closest-packed surface is most commensurate with the wavelength associated with the density pair correlation function of the disordered system. In practice, our result implies that the reinforcement of MGs is longest-lived for nanocrystals with close-packed surfaces.

---

‡ Corresponding author, e-mail: konglt@sjtu.edu.cn.

1. Introduction

Bulk metallic glasses (BMGs) have attracted great attention from both scientists and engineers in the past decades [1, 2, 3, 4, 5]. Their superior strength and hardness combined with an excellent resistance to corrosion and wear make them promising candidates for advanced structural applications. However, the brittleness of BMGs under ambient conditions limits their current use [1, 6, 7].To improve the situation, great efforts have been devoted to understanding the origin of their brittleness as well as to improving their ductility. It is now accepted that the macroscopic brittleness of BMGs originates from highly localized, heterogeneous deformations via the formation of shear bands [8]. The ductility of MG can be improved by introducing second-phase particles either *ex situ* [9, 10] or *in situ* [11, 12, 13, 14] into the MG matrix so as to hinder the propagation or homogenize the nucleation of shear bands.

As in other composites, one should expect the interface between embedded particles and the matrix to play a critical role for the macroscopic mechanical properties. Nevertheless, little is known about the interface between crystallites and the disordered, glassy matrix, This concerns in particular its microstructure, which is difficult to measure experimentally, because locating the interfaces remains a challenge. While atomistic computer simulations allow one to observe the (interfacial) microstructure directly – given sufficiently accurate potentials – most studies have so far focused on bulk systems, on interfaces between two glass regions [8, 15], or, the analysis was focused on the mesoscale interfacial morphology [16, 17], coarse-grained properties (density and elasticity) [18], or mechanical behavior [19, 20] rather than on the atomic-scale structure. Another aspect not yet investigated is the relevance of the orientation of the crystallites for the atomic-scale structure and its effect on interfacial properties. The objective of this study is to fill these gaps by providing a characterization of the interfacial atomic structure and by quantifying the dependence of some selected interfacial properties on the surface orientation of the crystal.

In this work, we report classical molecular-dynamics simulations of the interfaces between glassy and B2-phase $Cu_{50}Zr_{50}$, or simply, CuZr. The choice for this material is predominantly motivated by the following reasons: First, CuZr is a generic MG, which is well characterized, including its atomic-scale structure. Second, B2-phase CuZr crystallites have successfully been employed as reinforcements. Third, accurate potentials are readily available for this alloy making it possible to run simulations of sufficient size. To characterize local order, we use primarily the concept of radical Voronoi tessellation [21, 22, 23], which can be roughly described as a generalized construction of Wigner-Seitz cells. A resulting Voronoi polyhedron can be indexed by how many faces with a given number of edges live on its surface. This information is then used to rationalize how different crystal orientations can lead to different interfacial properties. We investigate width and roughness of the interface, as well as density oscillations near the crystal surfaces, but mainly focus on the interfacial energy and the crystallization activation energy. The latter is an important property primarily for *in-situ* precipitated nanocrystals, whose size can grow, sometimes to an unwanted large extend, upon heating or deformation [24, 25, 26, 27].

The remaining parts of this work are organized as follows: Section 2 describes the details of the models and the adopted simulation procedures as well as the characterization methods. Section 3.1 discusses the atomic structure of the interfaces, and section 3.2 presents the interfacial energies determined, while section 3.3 analyzes the crystallization kinetics of the interfaces. Finally, a summary is presented in Section 4.

2. Simulation details and characterization methods

Interactions between atoms were modeled with the embedded atom method (EAM) potential [28]. The parametrization by Cheng *et al.* [29, 30] for Cu-Zr alloys was chosen, because it successfully resolved the atomic structure of binary Cu-Zr and ternary Cu-Zr-Al MGs [29]. Molecular-dynamics (MD) simulations were carried out with the LAMMPS simulation package [31, 32]. Periodic boundary conditions were imposed in all three directions. The NpT ensemble was used [33, 34, 35], with damping constants of 2 ps and 20 ps for the thermostat and barostat, respectively. A time step of 2 fs was adopted.

Initial configurations consisted of an orthogonal supercell of perfect B2 CuZr crystal, with the desired crystalline planes, namely (100), (110), or (111), being parallel to the xy plane. The size of the as-set simulation box was around $55 \times 55 \times 110$ Å^3, containing about $20,000$ atoms in total. The system was first equilibrated under 300 K and 1 bar for 2 ns, and then divided into two parts of roughly equal size along the z direction. The temperature of one part was maintained at 300 K, while the other part was firstly heated up to $2,000$ K (which is far above the melting point of $\sim 1,200$ K for B2 CuZr) at a rate of 10^{11} K/s, maintained for 2 ns, and then quenched down to 300 K at a rate of 10^{11} K/s. The glass transition temperature of $\mathrm{Cu_{50}Zr_{50}}$ at this cooling rate was determined to be $T_\mathrm{g}(10^{11}$ K/s$) \approx 736$ K, below which the specific heat is strongly reduced. For half the cooling rate, we found a slightly reduced value of $T_\mathrm{g}(5\times10^{10})$ K/s ≈ 727 K. Incidentally, as a comparison, values of ~ 670 K were reported experimentally at a cooling rate several orders of magnitude lower than the simulated ones [36, 37]; the agreement between experimental result and simulation data provides further confirmation on the reliability of the employed potential and adopted simulation procedure. The whole system was then annealed at 300 K until the potential energy leveled off. This generally lasted 10 to 20 ns. During the whole procedure the pressure of the system was monitored at 1 bar with a Berendsen barostat [35].

The quenched configurations were heated back up from 300 K at a rate of 10^{10} K/s to a desired temperature, say 400 K, annealed for ∼50 ns at each temperature and then measurements were conducted in the following 20 ns. The procedure was followed by a second quench from 600 K to 300 K at a rate of 10^{10} K/s. Configurations during the second quench were stored at a step of 50 K which were relaxed at the corresponding temperature for at least 10 ns and measurements were taken over another 10 ns.

Three different amorphous-crystal interface (ACI) models with (100), (110), and

(111) surfaces of B2 CuZr being parallel to the interface respectively were considered. Fig. 1 illustrates a composite model containing a crystalline slab of around 50 Å in thickness sandwiched by amorphous slabs of about the same size. Due to the periodic boundary conditions, our simulation cell contains only one crystalline and one amorphous slab but two interfaces. The reliability of the interaction potential and that of the procedure to generate the amorphous phase are justified in Fig. 2 by a rather satisfactory agreement between the experimentally measured [38] and the MD-simulation based extended X-ray absorption fine structure (EXAFS) spectra.

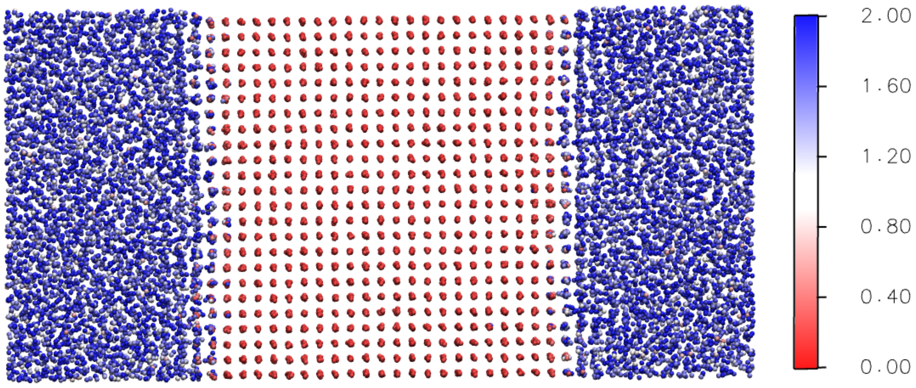

Figure 1. (Color online) Illustration of the interface model between amorphous $Cu_{50}Zr_{50}$ and B2 CuZr, with (110) of B2 CuZr in parallel to the interface. Balls, representing atoms, are colored according to their local order parameter (LOP) defined in Eq. (1). A small LOP indicates a close resemblance to a B2-phase like bonding environment.

A quantitative description of an interface including estimates for its location and width requires a suitable local order parameter (LOP), ϕ, to distinguish the local environment for a specific atom. To this end, several expressions have been proposed [40, 41, 42, 43]. For our work, we adopted an LOP similar to that employed by Hoyt *et al.* [43] with which they identified the solid-liquid interface in pure nickel. It measures the *minimal root-mean-square-deviation* (RMSD) of atoms – adjacent to a central atom – from ideal lattice positions of a reference lattice, which is defined on-the-fly for each central atom [43]. Specifically,

$$\phi \equiv \min\left(\sqrt{\frac{1}{N}\sum_{i=1}^{N}\left|\vec{r}_i - \vec{r}_i^{\,0}\right|^2}\right), \tag{1}$$

where N is the number of neighbors for the central atom – in the present case of B2 CuZr, we chose $N = 14$ to include the first two nearest-neighbor shells. $\vec{r}_i$ is the vector pointing from the central atom to its ith neighbor, while $\vec{r}_i^{\,0}$ is the corresponding lattice vector of the local reference crystal. The orientation of the reference crystal associated with a given atomic site is optimized through a minimization algorithm following that proposed by Kabsch [44]. A small LOP indicates a local structure similar to that of the B2 crystal, while a large value implies a large deviation from it. The LOP is roughly

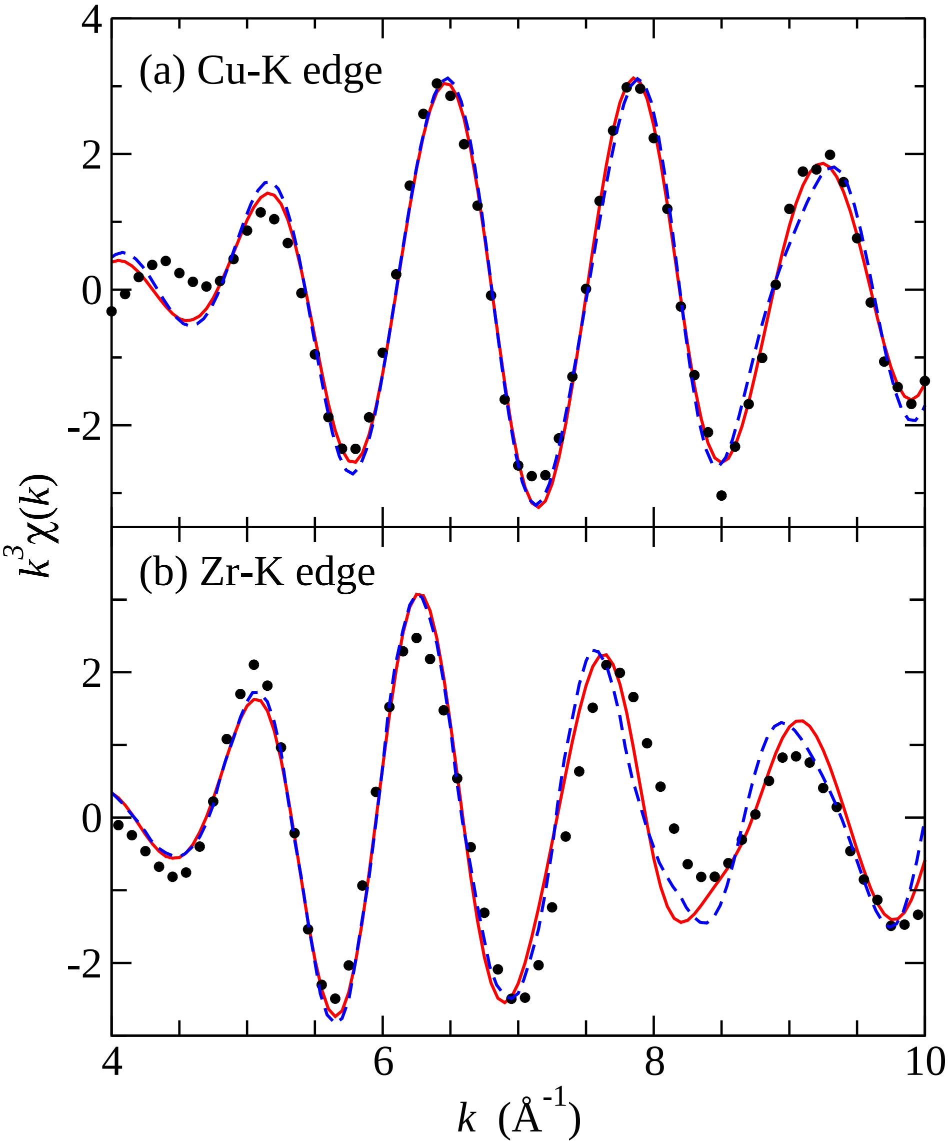

Figure 2. (Color online) Comparison of experimental EXAFS spectra of a CuZr BMG [38] indicated by (black) points with MD-based spectra ($T = 300$ K). The latter were obtained with the FEFF9 code [39] via an average over 500 configurations that were randomly chosen over the observation phase of a simulation. For each absorber, scattering from atoms up to the second nearest neighbors based on Voronoi tessellation was taken into account by path expansion [39]. Full (red) and broken (blue) lines are based on the equilibrated bulk $Cu_{50}Zr_{50}$ configurations at 300 K from the first and the second quench, respectively.

linearly dependent on temperature for a classical crystal, but even close to melting it takes lower values than in the amorphous phase at any temperature. To state orders of magnitude, the typical mean LOP in the amorphous phase at room temperature ($\phi_a \approx 1.8$ Å – precise numbers depend weakly on the thermal history) turns out more than ten times the mean LOP ($\phi_c \approx 0.16$ Å) in the crystal. As a consequence, it suffices to average over a few dozen atoms in order to obtain a meaningful, coarse-grained LOP. This allows us to bin our samples into thin segments of ~ 0.25 Å, while still producing a relatively smooth dependence of the coarse-grained LOP across the microscopically resolved interface. Unfortunately, this approach fails to provide information on whether a volume element contains predominantly a mixture of atoms in glass-like and crystalline-like coordination environments or "truly interfacial" atoms with bonding characteristics distinct from both glass and crystal.

The Voronoi tessellation method provides a means to characterize the local atomic packing topology [15, 21, 22, 23]. A central atom is assigned a polyhedral space that consists of all points in space being closer to the central atom than to any other atom. In the radical tessellation [23] used in this work, the distance to an atom is expressed in units of a size associated with this atom. Each Voronoi polyhedron and corresponding central atom can then be labelled by a set of indices $\langle n_3, n_4, n_5, n_6 \rangle$, where n_i denotes the number of i-edged faces of the polyhedron surrounding a central atom. For example, the Voronoi index for atoms in a B2 crystalline phase under low temperature is always $\langle 0, 6, 0, 8 \rangle$, as the Voronoi polyhedron surrounding each atom has 6 tetragons and 8 hexagons. $\langle 0, 0, 12, 0 \rangle$, representing an icosahedron cluster, is an abundant polyhedron in some amorphous alloys [45, 46]. The Voronoi index can therefore serve as a fingerprint characterizing the local topology of an atom as well as the local cluster containing the central atom and its neighbors. In order to reduce the errors introduced by thermal fluctuations, faces with very small areas and edges with very short lengths are ignored when labelling the Voronoi indices in this work.

3. Results and discussion

3.1. Interfacial structure

A first analysis of local order in our CuZr model is presented in Fig. 1. It shows an interface between the amorphous phase and the (110) surface of a B2 crystal. Owing to the color coding of atoms according to their LOPs, the crystalline domain can be readily located in Fig. 1. A sharp transition from the crystalline to the disordered phase with an interface can be seen. The (apparent) interface does not seem to have roughness beyond one or at most two (110) planes for the system size investigated here. While the absence of interfacial roughness is potentially related to the initially sharp transitions between hot and cool regions in our samples, we did not observe significant roughening when temperature was increased sufficiently much to allow for crystal growth at rates accessible for MD simulation. We therefore conclude that capillary waves do not play an important role at the scales investigated here.

In order to quantify location and width of an amorphous-crystalline interface, we analyse the coarse-grained LOP, $\phi(z)$, as a function of the coordinate z normal to the interface. As is seen from Fig. 3, $\phi(z)$ shows clear plateaus in the amorphous and crystalline phase, one can write the expectation value of $\phi(z)$ as

$$\langle \phi(z) \rangle = [\phi_{\mathrm{c}} - \phi_{\mathrm{a}}] \cdot S(z) + \phi_{\mathrm{a}}, \tag{2}$$

where $S(z)$ is a switching function taking the values zero in the bulk glass and one in the crystal. Moreover, ϕ_a and ϕ_c are the average LOP for the bulk glass and the pure crystal, respectively. As demonstrated in Fig. 3, $S(z)$ can be approximated quite accurately with

$$S(z) = \frac{1}{2}\left[\tanh\left(\frac{z - z_1}{W_\mathrm{LOP}}\right) - \tanh\left(\frac{z - z_2}{W_\mathrm{LOP}}\right)\right], \tag{3}$$

where the adjustable parameters z_1 and z_2 give the location of the interface, while W_LOP is a first measure for the interfacial width.

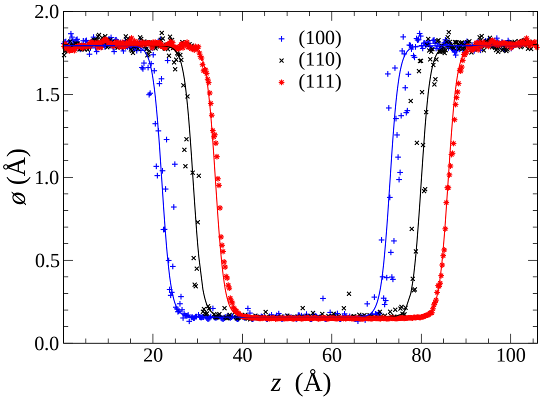

Figure 3. (Color online) Coarse-grained LOP $\phi(z)$ as a function of the coordinate z normal to the interface for ACI (100), (110), and (111). The central region is the crystalline part, while the outer regions correspond to the amorphous part. Symbols represent simulation results, while lines are fits according to Eqs. (2) and (3). Different data sets are shifted along the z-axis to improve their visualization.

From the fits shown in Fig. 3, one would deduce very small interfacial widths barely exceeding the corresponding crystalline interlayer spacings. Values are listed in Table 1 together with other interfacial and bulk properties. Our estimates for the interfacial widths are similar to those by Kokotin *et al.* [18] who studied $Cu_{47.5}Zr_{47.5}Al_5$ rather than $Cu_{50}Zr_{50}$. They found widths of approximately 0.3 nm by exploiting an apparent density reduction of the interphase compared to the bulk glass. (Here, we use the term “interphase” to describe the state of material in the thin zone between MG and crystal.) However, their analysis was based on a multi-faceted nano-crystal embedded into an amorphous environment. Such a geometry makes it difficult to observe subtleties of extended interfaces. For example, density oscillations, which one would expect for a high-density fluid or glass near a confining wall, remain unnoticed. Moreover, the presence of many edges can induce a reduction of density of the interphase compared to our geometry. This is why the dip in density between the crystalline and the bulk amorphous region might have been caused by the particular set-up rather than be an intrinsic property of the interphase.

In order to investigate to what degree density-based and LOP-based estimates for the interfacial width agree, we computed a coarse-grained density $\rho(z)$ using similar

Table 1. Various bulk properties including those of the interphase. Here, (100) refers to the (inter)phase sandwiched between a MG and a (100) surface of a B2 crystal. $\langle\phi\rangle$ is the mean value of the LOP and W_{LOP} the LOP-based estimate for the interfacial width, while W_ρ and W_{V} are based on the analysis of the decay of density oscillations and the Voronoi analysis, respectively. $\overline{V}$ indicates the mean Voronoi volume per atom.

Phase	B2	glass	(100)	(110)	(111)
$\langle\phi\rangle$ (Å)	0.16	1.80	1.30	1.12	1.10
$\overline{V}$ (Å^3)	17.57	17.83	17.74	17.75	17.73
$\overline{V}_{\mathrm{Cu}}$ (Å^3)	13.21	12.90	13.09	13.14	13.14
$\overline{V}_{\mathrm{Zr}}$ (Å^3)	21.92	22.76	22.49	22.36	22.32
W_{LOP} (Å)	N.A.	N.A.	2.39	1.76	2.49
W_ρ (Å)	N.A.	N.A.	3.08	5.05	3.26
W_{V} (Å)	N.A.	N.A.	9.09	7.95	9.03

bins as for the calculation of $\phi(z)$. The density profiles, which are shown in Fig. 4, were fitted again with a hyperbolic switching function. This time, the cosine fluctuations needed to be incorporated leading to the following fitting function for the left interface:

$$\rho(z) = \left[\rho_{\mathrm{C}} - \rho_{\mathrm{A}} + \Delta\rho \cos\left(2\pi\frac{z}{d} + \varphi\right)\right] \cdot H(z) + \rho_{\mathrm{A}}, \tag{4}$$

$$H(z) = \frac{1}{2}\left[1 + \tanh\left(\frac{z - z_0}{W_\rho}\right)\right], \tag{5}$$

where ρ_{A} and ρ_{C} are the average atomic densities in the amorphous and crystalline part, respectively. The interlayer spacings in the crystal are denoted by d. They are 1.64, 2.32, and 0.95 Å for ACI (100), (110), and (111), respectively, in accordance with the respective distances in bulk B2 CuZr. Thus, the remaining (fitting) parameters are $\Delta\rho$, which is the fluctuation amplitude in density profile, the approximate location of the interface z_0, a phase shift φ, and a new estimate W_ρ for the width of the interface between crystalline and non-crystalline domains. Numerical results for W_ρ are included in Table 1.

Several points are worth discussing in relation to the density oscillations and the results for W_ρ: (1) It is not meaningful to ascertain an average density of the interface from Eq. (4), because $\Delta\rho$ is much larger than the density difference between the various phases. We return to the analysis of atomic volume (and thus density) in the context of the Voronoi tessellations. (2) The density oscillations of the crystal penetrate into the disordered phase and they do this with a decay length exceeding the LOP-based estimate for the interfacial width. More importantly, W_{LOP} and W_ρ are not linearly related. As can be seen in Table 1, the difference between W_ρ and W_{LOP} is almost a factor of three for the (110) orientation, while it is approximately 1.3 for the other two studied interfaces. This is a quite significant orientation dependence. (3) High-density simple fluids, including binary mixtures, show pair correlation functions whose asymptotic decay is given by a single, complex correlation length that is a temperature-

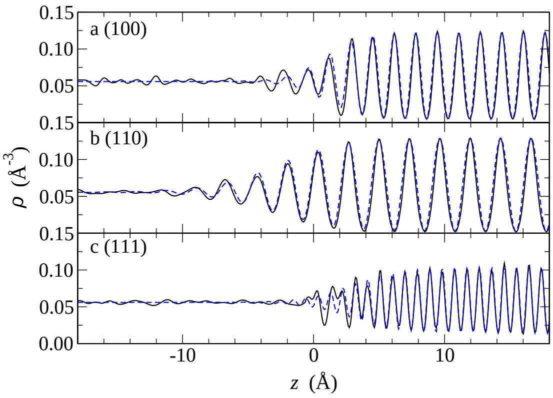

Figure 4. (Color online) Atomic number density (ρ) profiles for ACI (100) (a), (110) (b), and (111) (c) at 300 K. The black solid lines represent the measured and smoothed profiles, while the blue dashed lines are fits to the data based on Eq. 4.

dependent, intrinsic property of the bulk fluid. Thus, for our system of interest, the effect of confining walls cannot be cast in terms of simple geometric constraints, as is frequently done in the analysis of the glass transition in confinement [47]. However, our observation of crystal orientation-dependent density profiles in the fluid, was to be expected, as we next discuss.

It is well-known that density oscillations of the solid can induce layering oscillations within an adjacent liquid with a periodicity of the solid interlayer spacing. For example, layering similar to that shown in Fig. 4 has been found for solid-liquid interfaces of related substances [48, 49, 50, 51, 52] and observed experimentally in an interface between crystalline Pd_3Si and amorphous $Pd_{80}Si_{20}$ [53]. If the periodicity of the density oscillation in the crystal is close to the natural periodicity of the liquid, the oscillations will survive a farther distance into the liquid than for large deviations [48, 54]. Thus, the layering can be interpreted in terms of “a density oscillation resonance.”

The concept of density oscillation resonance for liquid-crystal interfaces are consistent with our results for orientation dependence of the density correlation length W_ρ. The natural periodicity of the liquid, d_l, is given by the inverse of the first peak position of the liquid structure factor, $2\pi/Q_0$. For $Cu_{50}Zr_{50}$ metallic glass, which can be seen as a supercooled liquid, it is located at $Q_0 = 2.65$ Å^{-1} corresponding to a natural periodicity of $d_\mathrm{l} = 2\pi/Q_0 \simeq 2.37$ Å. Thus, the 2.32 Å interlayer spacing for (110) layers of B2 CuZr is only 2% smaller than d_l. As a consequence, density oscillations decay less quickly away from a (110) surface than for orientations with less favorable spacings. In our case, $d_{(100)} = 1.64$ Å is reduced with respect to d_l by 31% and $d_{(111)} = 0.95$ Å by 60%. For the (111) interface, one can barely see any imprint of the crystalline density oscillation into the disordered part. It even seems as if there is an interference effect in the profiles, potentially induced by the interphase trying to find a compromise between picking up the density oscillation from the bulk and imposing its own preferred layering,

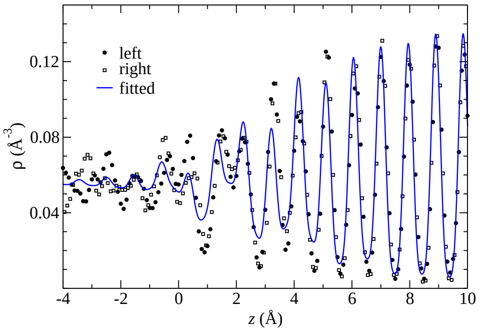

Figure 5. (Color online) Fit of the density profile of a (111) interface that includes a wavelet with spacing identical to the intrinsic spacing of the fluid density correlation function. The right interface is flipped and shifted such that its density profile overlaps with that of the left interface.

which it would adopt in front of a perfectly-flat, "mathematical" wall.

To test this last hypothesis we refitted the density profile for the (111) interface by including a wavelet to the density profile such that adjacent extrema of the wavelet are spaced by d_l, i.e., we added

$$\Delta\rho_l = \Delta\rho_l^0 \cos\left[\frac{2\pi}{d_\mathrm{l}}(x - x_\mathrm{l})\right] I(z), \tag{6}$$

to the density function described in Eq. (4). Here, the prefactor ρ_l^0 and the phase term $2\pi x_\mathrm{l}/d_\mathrm{l}$ are adjustable parameters, while $I(z)$ is an interfacial switching function, which will be introduced further below in Eq. (8). For d_l, the experimental value is used without adjustment. Fig. 5 reveals that the added wavelet allows one to reproduce many features of the seemingly erratic behavior of the (111) density profile.

In summary of the above discussion, one may state that the (110) orientation, having the largest-spaced layers and the most dense-packed surfaces, accommodates the MG the best in the sense that it allows the disordered system to develop the density oscillation that it intrinsically "wants" to have. This should imply that this orientation is energetically or thermodynamically the most stable one. The closer-spaced the layers and thus the less-dense the surfaces, the more the disordered system needs to find a compromise between its intrinsic and the externally-imposed density oscillations. This should mean a reduced stability. However, since W_LOP and W_ρ are orientation-dependent, and moreover, both LOP and density have little contrast between the interphase and the MG, one needs additional criteria to identify a meaningful interfacial width.

Compared to the local-order parameter or the coarse-grained density, the tessellation analysis gives more insight into local symmetry and bonding. To illustrate different local geometries, we show selected Voronoi polyhedra representative for the MG (a), the interphase (b-e), and the crystal (f) in Fig. 6. In the two bulk phases, MG and crystal, the Voronoi-polyhedra distributions are well defined, at least given the thermodynamic reference point. Almost every polyhedron in the crystal is $\langle 0, 6, 0, 8\rangle$, unless in the vicinity of a defect or for a brief moment in time due to a large thermal fluctuation. In the case of the MG, the thermal history can and does influence details in the Voronoi distribution function. However, despite certain subtleties, we find – in agreement with a careful, combined numerical and experimental study by Li *et al.* [55] – that the MG always has a relatively large number of Voronoi polyhedra with five-edged faces.

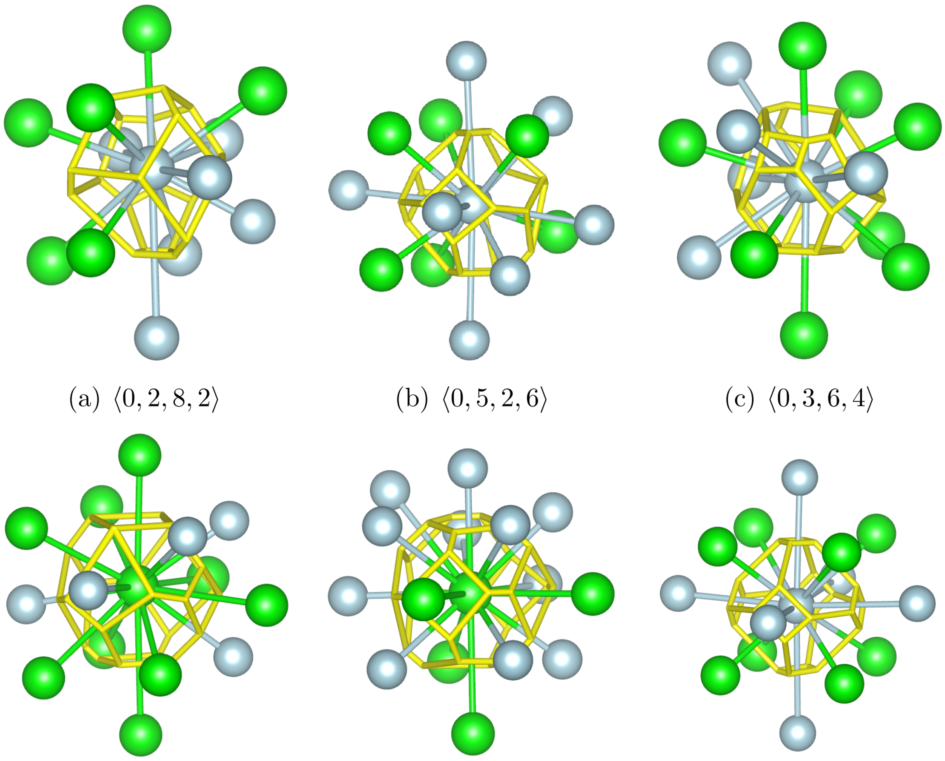
(a) $\langle 0,2,8,2\rangle$ (b) $\langle 0,5,2,6\rangle$ (c) $\langle 0,3,6,4\rangle$

(d) $\langle 0,4,4,6\rangle$ (e) $\langle 0,5,2,8\rangle$ (f) $\langle 0,6,0,8\rangle$

Figure 6. Illustration of frequently occurring Voronoi clusters. The cyan balls represent Cu atoms, while the green ones are Zr. Yellow cages outline the corresponding Voronoi polyhedron surrounding the central atom.

To estimate the points beyond which the system can be classified as bulk MG, we need a second order parameter, i.e., one that is sensitive to the structural differences in the MG and the interphase. In analogy to the switching function $S(z)$ for the crystal, we define a "MG weight function", which takes the value one within the MG and zero, or at least close to zero, outside of it:

$$G(z) = \frac{1}{2}\left[\tanh\left(\frac{z-z_2}{w}\right) - \tanh\left(\frac{z-z_1}{w}\right) + 2\right], \tag{7}$$

Note that $G(z)$ is not simply the complimentary of $S(z)$: the parameters $z_{1,2}$ and w in Eq. (7) characterize the boundary of the MG, while they relate to the crystalline boundary in Eq. (3). However, we still need an observable, such as the LOP in Eq. (2), to identify a MG domain. We explored several possibilities, including the number of five-edges faces per atom, but found it best to count the relative number of Voronoi polyhedra that almost exclusively occur in the MG. These were Cu centered $\langle 0,2,8,2\rangle$, $\langle 0,2,8,1\rangle$,

$\langle 0,0,12,0\rangle$, and Zr centered $\langle 0,2,8,5\rangle$, $\langle 0,1,10,4\rangle$. To also base the analysis of local order in the crystal onto tessellations, we counted the relative number of $\langle 0,6,0,8\rangle$ polyhedra. This is the new order parameter used to identify structures being locally similar to that of the B2 crystal.

In Fig. 7(a), we demonstrate for a (110) ACI that the MG-sensitive order parameter decreases before the B2-crystal-sensitive parameter starts to pick up, and vice versa. In addition, Fig. 7(b) reveals that certain Voronoi polyhedra only occur with non-negligible likelihood outside the bulk MG and the crystal. This means that the interphase between MG and B2 has its own structural characteristics. Nevertheless, it does not appear meaningful to define an independent "interphase order parameter", at least based on Voronoi tessellations, because the interphase is a gradient structure. We therefore define the interphase as a lack of both MG and B2 order, and thus introduce the interphase weight function as

$$I(z) = |1 - [S(z) + G(z)]\,|. \tag{8}$$

As can be seen in Fig. 7(b), $I(z)$ correlates with an increased occurrence of certain Voronoi polyhedra. The width W_V over which they can be seen is quite accurately twice the full width at half maximum (FWHM) of the $I(z)$ peak. This is why we chose the latter as the measure for the Voronoi-based width W_V of the interfacial domain.

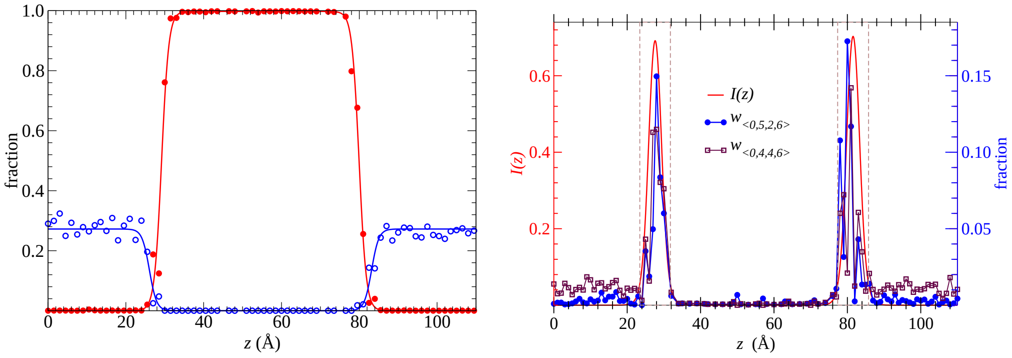

(a) (b)

Figure 7. (a) Fraction of Voronoi polyhedra characteristic for the MG (filled, red circles) and the B2 crystal (open, blue circles) as a function of the coordinate normal to the interface. (b) Fraction of polyhedra characteristic for the interphase. The red curve is based on Eq. (8), where the functions $S(z)$ and $G(z)$ were obtained by fits to the data shown in (a). The vertical dashed lines in (b) indicate the interfacial region as given by twice the FWHM of the corresponding peak.

Analyses similar to that shown in Fig. 7 were conducted for the (100) and (111) ACIs. Characteristics resembled those of the (110) ACI, for example, $\langle 0,5,2,6\rangle$ polyhedra centered on interfacial Cu and $\langle 0,4,4,6\rangle$ polyhedra on interfacial Zr, are most abundant besides $\langle 0,6,0,8\rangle$, as is evidenced in Fig. 8. The distributions depend only slightly on the orientation of the crystals. In most cases, the relative differences between the populations are less than 1% in absolute or 10% in relative numbers.

Only few tessellations deviate from this rule, e.g., the $\langle 0,4,4,6\rangle$ polyhedra seem to be particularly abundant for the (110) ACI. Given the similarity of the Voronoi tessellation distributions for different orientations, one would expect only a small dependence of the energy density in the different interphases, in particular as the energy depends primarily on local properties in the EAM model.

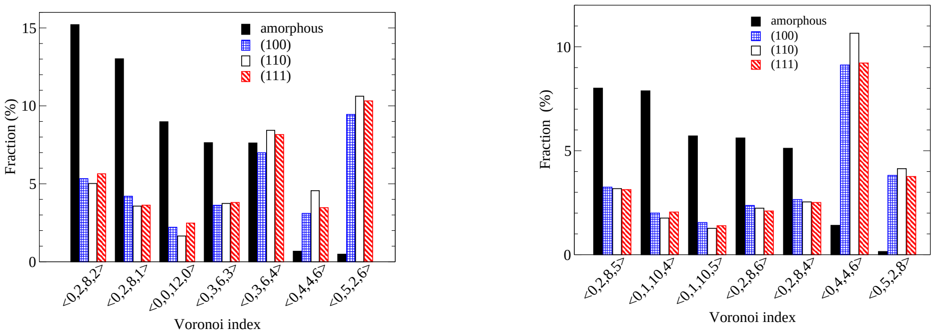

(a) (b)

Figure 8. Comparison of the fractions of the most abundant Voronoi polyhedra in the bulk amorphous and the interfacial regions: (a) for polyhedra centered on Cu atoms, and (b) for those centered on Zr atoms.

So far, we presented analyses of samples that had been produced by quenching liquid $Cu_{50}Zr_{50}$ from the melt to ambient temperature. The employed rates were orders of magnitude larger than in experiment so that the produced kinetically-trapped, metastable states risk to have different characteristics from those relevant to experiment. Thus, despite the nice similarity of experimental and MD-based EXAFS structure factors in Fig. 2, we would like to produce further (self-consistent) evidence in this work that structural relaxation does not alter the *trends* reported in this study so far. Towards this end, we anneal the systems at elevated temperature, which speeds up structural relaxation to an extent that it can be observed on time scales accessible to MD, and then quench it back down as described in the method section. Selected results are presented in Fig. 9.

Fig. 9 reveals that annealing indeed changes the fractions of Voronoi polyhedra populations in the interfacial region. However, this happens such that the relative changes are similar for all three investigated ACIs. For example, the number of $\langle 0,5,2,6\rangle$ polyhedra increases by a little more than 1% (in total, not relative) for each ACI, while that of $\langle 0,3,6,4\rangle$ decreases by a similar amount. Other polyhedra fractions, not shown explicitly, show analogous behavior. When quenching the system back down to 300 K, the fractions of the different polyhedra assume similar values as during heating. It therefore seems as though the interfacial structure is predominantly a function of temperature and surprisingly insensitive to the thermal history. The bulk glass shows similar trends, although increases in the fraction of the $\langle 0,0,12,0\rangle$ appear to be irreversible in the glass.

We complete this section with a short discussion of the interphase density including

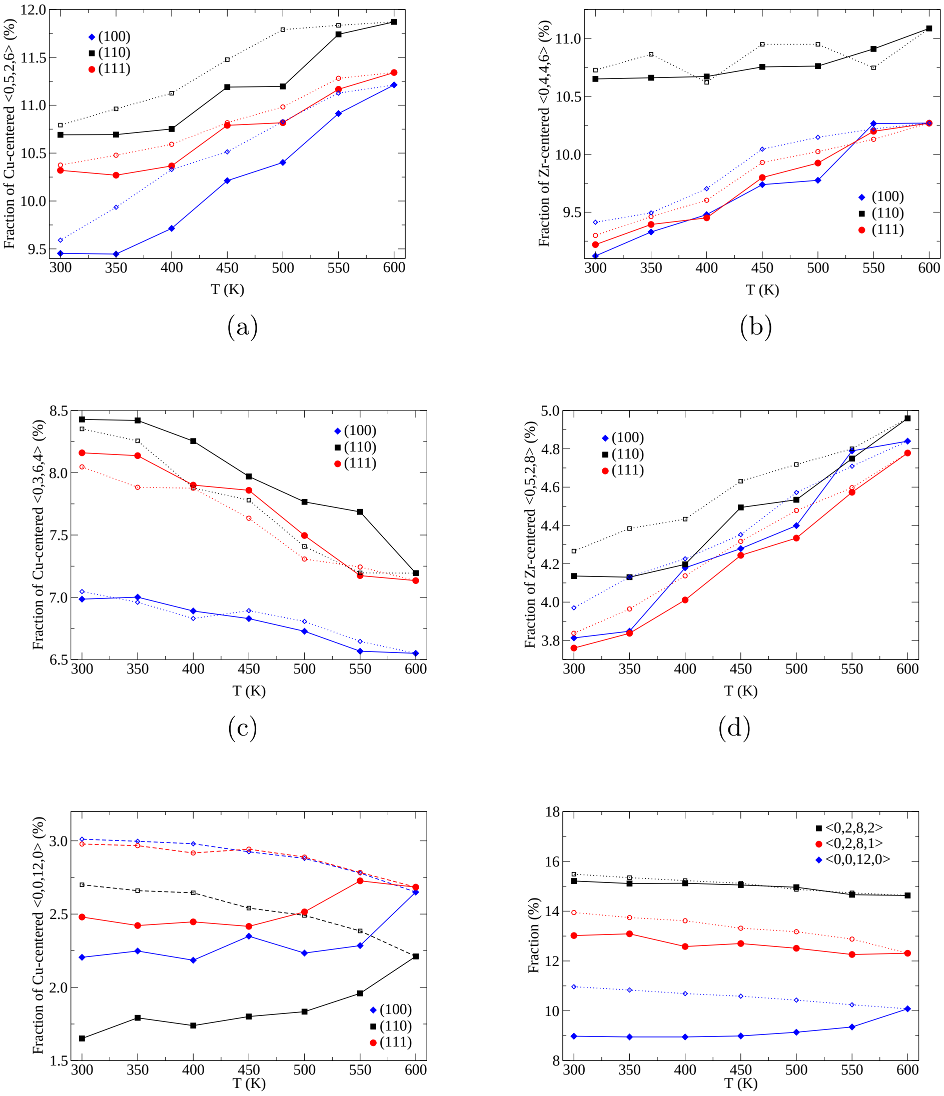

(a) (b)

(c) (d)

(e) (f)

Figure 9. Variation of Voronoi polyhedra content in the interfacial region (a)-(e) and the glass (f) as a function of annealing temperature for ACI (100), (110), and (111). Solid lines refer to the heating simulations, while dotted lines represent the second quench.

a characterization of some frequently-occurring Voronoi polyhedra. The density, or alternatively, the mean volume of atoms in the interphase, see Table 1, was determined by averaging the Voronoi volume associated with each atom type. In contrast to other properties, we find almost no dependence on the orientation of the crystalline surface. For all three ACIs, the average volume per atom in the interface turns out to be in between that of the crystal and that in the bulk glass. The alloy achieves a high packing at the interface and the smooth transition between B2 and MG by forming defective B2 polyhedra. Specifically, the alloy attempts to have more four and/or six-edges faces on the crystalline side (depending on the surface termination) while having more five-edged faces on the glassy side. This can be done with rather dense polyhedra. For example, the Cu-centered $\langle 0,5,2,6\rangle$ polyhedron, which is particulary frequent in the (110) ACI, only has one neighbor less than the B2 motif $\langle 0,6,0,8\rangle$. Its average volume of 13.07 Å^3 is relatively small compared to 13.14 Å^3 of all Cu atoms in the interfacial region of ACI (110). The frequent interfacial Zr-centered $\langle 0,4,4,6\rangle$ can also be derived from the high-density $\langle 0,6,0,8\rangle$, i.e., by introducing substitutional rearrangement of nearest-neighbor atoms. This leads again to a rather small volume of 22.15 Å^3, which is smaller than the radical-Voronoi tessellation based average volume for Zr in the MG of 22.76 Å^3.

Given that different crystal surfaces have different terminations, it seems obvious that the interfacial structures need to be orientation dependent. However, given the similarity of the Voronoi tessellation distribution and average volume per atom for different ACIs, the effect could be small. The influence of the crystal orientation on thermodynamic and kinetic properties is investigated in the next two sections.

3.2. Interfacial energy

The interfacial energy (γ) is the excess free energy due to the presence/creation of an interface separating two coexisting phases at equilibrium. The larger γ, the less strong are the bonds between the two phases. Therefore, the interfacial energy is an important parameter for the stability of an interface, which is why it is of great concern in the development and application of composite materials. In theory, the difference in Gibbs free energy under constant pressure includes an internal energy contribution, an entropic and a volumetric contribution. The latter two terms are generally small for hard condensed matter systems at ambient conditions. Since entropic contributions are notoriously difficult to ascertain (in particular those contributions going beyond vibrational entropy), we approximate the interfacial potential energy by the mean interfacial energy. In practice, γ can be evaluated mathematically as the excess potential energy of a system containing an interface compared to a weighted sum of the two constituent phases [56, 57]:

$$\gamma \approx \frac{E - N_{\mathrm{c}}e_{\mathrm{c}} - N_{\mathrm{a}}e_{\mathrm{a}}}{A}, \tag{9}$$

where E is the total energy of a sample containing an interface, N_{c} and N_{a} are the number of crystalline and amorphous atoms in the sample, e_{c} and e_{a} are the average atomic potential energy in pure crystalline or pure amorphous phase, respectively, and A is the interfacial area. In our case, A corresponds to twice the cross-sectional area of the simulation cell, as we have two interfaces in the (minimum image of our) simulation cell.

Obviously, the evaluation of γ requires the determination of N_{c} and N_{a}, i.e., we need to identify the crystallographic environment for each atom. This is non-trivial in the present case, as atoms cannot always be unambiguously associated with either phase, all the atoms in the interphase have bonding characteristics distinct from both

B2 and MG. Despite of this difficulty, we explored different schemes to obtain well-defined and meaningful values for N_c and N_a. All schemes lead to similar results. The analysis presented here was based on labeling atoms as crystalline if their average local LOP was less than the threshold value of $\phi^*_\mathrm{LOP} = 0.56$ Å. This particular choice is motivated by the observation that the distribution histograms of LOP for all ACIs have two distinct peaks, which corresponds to the bulk crystalline and glassy region respectively, and a threshold of $\phi^*_\mathrm{LOP} = 0.56$ Å will separate these two peaks reasonably well in all situations considered in this work. In contrast to N_c and N_a, the terms e_c and e_a are straightforward to evaluate by averaging the respective energies per atom for bulk systems. In case of the MG, the bulk system must have undergone the same thermal history as that of the glass region of the ACI.

With the just-described procedure, we evaluate the interfacial energies for ACI (100), (110), and (111) at room temperature to be 190, 165, and 172 mJ/m^2, respectively. Choosing different criteria for the estimate of N_c shifts our numerical values by $O(10$ mJ/m$^2)$, but differences between the crystal orientations remain well below 2 mJ/m^2. To provide a single characteristic surface energy, we employ an averaging scheme proposed by Davidchack *et al.* [58], $\gamma_0 = (10\gamma_{100}+16\gamma_{110}+9\gamma_{111})/35$, which yields $\gamma_0 = 174$ mJ/m^2. This value is of the same order as that proposed for a (Cu)crystal-(Cu/Zr)amorphous interface by Huang *et al.* [59], who arrived at a value of 202 mJ/m^2 but twice as large as similar estimates for glass-glass interfacial energies in $\mathrm{Cu}_{64}\mathrm{Zr}_{36}$. Our result for γ_0 is also consistent with an empirical observation for solid-liquid interfacial energies γ_sl postulated by Turnbull [60]. He found that the dimensionless coefficient $\alpha = \gamma_{sl}/(L\rho^{2/3})$ varies little for different materials, e.g., it typically lies between 0.27 and 0.36 for BCC metals [61, 62, 63]. Here, L is the latent heat and ρ the atomic number density in the solid. Although the structure relaxation in the interface model is far from being finished yet, variation in the interfacial energy is expected with further annealing of the interface, it is however of interest to compare the present result to the Turnbull equation by interpreting the amorphous phase in the present study as a supercooled liquid. Our Turnbull coefficient turns out to be $\alpha = 0.31$, which is well within the range of values reported for BCC metals. These two comparisons suggest that our interfacial energies are reliable, although the entropic and volumetric contributions to γ are neglected. However, in comparison to crystal-liquid interfaces [63], we find a relatively large orientation dependence, i.e., the relative differences between γ_{100} on one side and γ_{110} and γ_{111} on the other side exceeds 10%. This is one order of magnitude larger than differences for BCC crystal-liquid interfaces [63].

As in the case of structural changes, we need to investigate to what extent the results for the interfacial energy change upon heating and subsequent annealing. Results are reported in Fig. 10. One sees that the interfacial energies decrease as temperature increases, while the orientation dependence of the interfacial energies is maintained. Interestingly, the relative changes between 300 K and 500 K are of order 10%. This is similar to that observed in the Voronoi tessellation populations. It is tempting to argue that this correlation is not fortuitous: The higher temperature increases the atomic mobilities allowing them to perform structural relaxations (reflected in altered Voronoi tessellation distributions), which enhance the locking between MG and crystal surfaces. When the temperature exceeds 500 K, crystallization starts to set in. This induces a small drift in N_c, which in turn makes it difficult to determine a well-defined γ with sufficient accuracy.

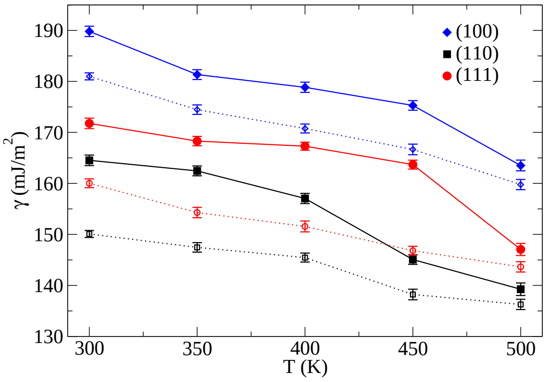

Figure 10. Variation of the interfacial energy for the ACI models as a function of temperature. Solid lines refer to the heating simulations, while dotted lines represent the second quench.

3.3. Crystallization kinetics

Metallic glasses are non-equilibrium materials and therefore change their structure with time. The structural relaxation can even lead to crystallization when the system is annealed sufficiently long. The higher the temperature, the less time it takes for crystallization to occur, at least for temperatures below the recrystallization temperature. On the time scales accessible to MD, crystallization can be observed when heating the ACI models to temperature above 500 K. The presence of a crystalline nucleus turns the crystallization process into a migration of the interface. Upon annealing at the elevated temperatures, the number of atoms identified as in the B2 phase increases continuously: atoms previously associated with the interphase become associated with the B2 phase and atoms initially belonging to the MG start becoming interfacial atoms, etc. The migration of the interface can be readily monitored with any of the parameters introduced in the last section resulting in essentially indistinguishable results for the crystallization rate v. The latter is defined as the number of atoms transformed from amorphous to crystal per unit time and cross-section area. As shown in Fig. 11, v follows an Arrhenius law

$$v = v_0 \exp\left(-\frac{Q}{RT}\right), \tag{10}$$

where v_0 is a prefactor, which is approximated as independent of temperature, Q is the crystallization activation energy, while R and T are the gas constant and the annealing temperature, respectively.

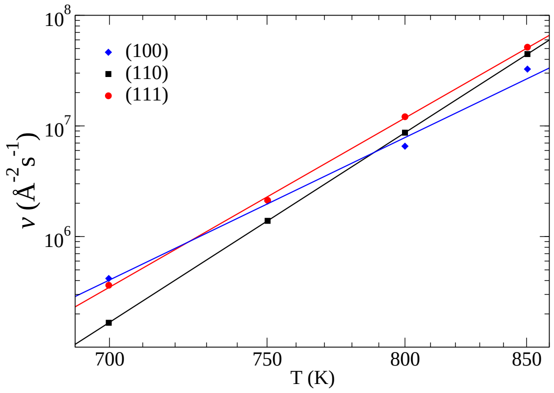

Figure 11. Crystallization rate as a function of temperature. Points are measured data, while the lines are the corresponding Arrhenius fittings.

Fig. 11 reveals that the crystallization rate is dependent on the orientation, just like the other properties investigated in the present study. The activation energies are determined by fitting the evaluated data to the Arrhenius equation, resulting in $Q = 138$, 166, and 164 kJ/mol for ACI (100), (110), and (111), respectively. Thus, the (110) ACI is the most stable interface, at least at small temperatures and the (100) ACI appears to have the smallest activation energy. The difference between Q_{110} and Q_{100} is similar in magnitude and opposite in sign to the differences in surface energies γ_{110} and γ_{100}. Such a correlation can be explained with the argument that a well-relaxed interphase needs more energy to reach the transition state, from where it can descend into the crystalline ordering. However, the phenomenological concept relating relaxation to free-volume cannot be employed in the present context, as all three ACI models have essentially identical mean volume per atom.

A possible explanation for why the closest-packed surface yields the most stable interface is that the (110) layers are separated by a distance that is almost identical with the period d_l of the density oscillations in liquid CuZr. The interphase can thus pick up the density oscillations from the crystal and simultaneously those of the disordered phase. For the intermediately close-packed (100) surface, the crystal density oscillations are still imprinted into the interphase, but the spacing differs from d_l by a substantial amount. The distance between (111) layers, the least closed-packed investigated here, is so small that there are barely density oscillations extending from the crystal into the interphase. Instead, the interphase shows density modulations that can be interpreted as intrinsic fluid modulations. These modulations may be energetically favorable, which would explain why the (111) interface is more stable than (100). It might be interesting to test these hypotheses by extending density-functional theories formulated for a hard-sphere melt-solid interface [64] to systems of higher complexity, such as CuZr.

Our results on the activation energy agree reasonably well with the experimental result by Lad *et al.*. They found $Q = 132$ kJ/mol for $Cu_{50}Zr_{50}$ metallic glass [65]. Also the orientation dependence is consistent with previous results. Shi *et al.* once revealed that the crystal growth rate along the [100] direction is greater than that along the [110] direction when compressing a $Cu_{50}Zr_{50}$ composite containing B2 nano-crystals [66].

4. Conclusions

In this work, we studied structure, energetics, and kinetics of nominally flat interfaces between amorphous $Cu_{50}Zr_{50}$ and B2 structured crystalline CuZr. Most investigated properties had an ascertainable dependence on the orientation of the crystalline surfaces including interfacial energy and the rate of crystallization. For example, we found that the interface with the closest-packed surface, namely (110) produced the most stable interface with the lowest surface (internal) energy and the lowest rate of crystallization at small temperature. However, the least closed-packed surface (111) turned out more stable than the (100) surface with intermediate packing. Thus, one cannot simply conclude that the stability of the interface correlates with the close-packing of the surface even if the origin of differences in surface energy must certainly be related to structural differences between different materials of identical chemical stoichiometry.

Our simulations revealed that the atomic-scale structure of the interphase between the MG and the B2 phase had its own characteristics. For example, some structural motifs, as characterized by Voronoi tessellations, occur with much higher probability in the interphase than in the MG or the crystal. The width W_V over which the structural motifs in the interphase differ from those in the MG or the crystal extends over roughly 8 to 9 Å. However, W_V does not correlate very well with surface or activation energies. W_V is largest (by 10%) and almost identical for (111) and (100). However, the interfacial and activation energies are similar for (111) and (110) but $O(10\%)$ less than those for (100). Moreover, there is no unique measure for the interfacial width. Depending on the investigated property (depth with which density oscillations penetrate from the crystal into the disordered phase, local order parameter measuring the similarity to local bonding in the crystal) different interfacial widths are obtained that show no obvious correlation to each other or interfacial and activation energies. We thus can still not answer the question why there is no systematic trend with the close-packing of a surface and the stability of the interface.

Acknowledgments

This work was supported by the National Natural Science Foundation of China (51001073, 51271114), Shanghai Pujiang Program (10PJ1405900), and State Key Development Program for Basic Research of China (2011CB610405). Computational resources from Jülich Supercomputer Center and Center for HPC at Shanghai Jiao Tong University are also acknowledged.

References

[1] C.A. Schuh, Todd C. Hufnagel, and Upadrasta Ramamurty. Mechanical behavior of amorphous alloys. *Acta Materialia*, 55:4067–4109, 2007.

[2] Morgana Martin Trexler and Naresh N. Thadhani. Mechanical properties of bulk metallic glasses. *Progress in Materials Science*, 55:759–839, 2010.

[3] Shin Takeuchi and Keiichi Edagawa. Atomistic simulation and modeling of localized shear deformation in metallic glasses. *Progress in Materials Science*, 56:785–816, 2011.

[4] A. Inoue and A. Takeuchi. Recent development and application products of bulk glassy alloys. *Acta Materialia*, 59(6):2243–2267, 2011.

[5] W. H. Wang. Bulk metallic glasses with functional physical properties. *Advanced materials*, 21(45):4524–4544, 2009.

[6] A. R. Yavari, J. J. Lewandowski, and J. Eckert. Mechanical properties of bulk metallic glasses. *MRS Bulletin*, 32:635–638, 2007.

[7] Golden Kumar, Amish Desai, and Jan Schroers. Bulk metallic glass: The smaller the better. *Advanced Materials*, 23(4):461–476, 2011.

[8] Karsten Albe, Yvonne Ritter, and Daniel Şopu. Enhancing the plasticity of metallic glasses: Shear band formation, nanocomposites and nanoglasses investigated by molecular dynamics simulations. *Mechanics of Materials*, 67:94 – 103, 2013.

[9] F. Szuecs, C.P. Kim, and W.L. Johnson. Mechanical properties of $Zr_{56.2}Ti_{13.8}Nb_{5.0}Cu_{6.9}Ni_{5.6}Be_{12.5}$ ductile phase reinforced bulk metallic glass composite. *Acta Materialia*, 49(9):1507–1513, 2001.

[10] D. Şopu, Y. Ritter, H. Gleiter, and K. Albe. Deformation behavior of bulk and nanostructured metallic glasses studied via molecular dynamics simulations. *Phys. Rev. B*, 83:100202, 2011.

[11] C.C. Hays, C.P. Kim, and W.L. Johnson. Improved mechanical behavior of bulk metallic glasses containing in situ formed ductile phase dendrite dispersions. *Mater. Sci. Eng. A*, 304-306(1-2):650–655, 2001.

[12] K. B. Kim, J. Das, F. Baier, M. B. Tang, W. H. Wang, and J. Eckert. Heterogeneity of a $Cu_{47.5}Zr_{47.5}Al_5$ bulk metallic glass. *Applied Physics Letters*, 88(5):051911, 2006.

[13] A. Inoue, W. Zhang, T. Tsurui, A. R. Yavari, and A. L. Greer. Unusual room-temperature compressive plasticity in nanocrystal-toughened bulk copper-zirconium glass. *Phil. Mag. Lett.*, 85(5):221–229, 2005.

[14] D. V. Louzguine-Luzgin, A. Vinogradov, A.R. Yavari, S. Li, G. Xie, and A. Inoue. On the deformation and fracture behaviour of a Zr-based glassy alloy. *Philosophical Magazine*, 88(23):2979–2987, 2008.

[15] Yvonne Ritter, Daniel Şopu, Herbert Gleiter, and Karsten Albe. Structure, stability and mechanical properties of internal interfaces in $Cu_{64}Zr_{36}$ nanoglasses studied by MD simulations. *Acta Materialia*, 59(17):6588 – 6593, 2011.

[16] K. X. Liu, W. D. Liu, J. T. Wang, H. H. Yan, X. J. Li, Y. J. Huang, X. S. Wei, and J. Shen. Atomic-scale bonding of bulk metallic glass to crystalline aluminum. *Appl. Phys. Lett.*, 93:081918, 2008.

[17] M.C. Liu, J.C. Huang, Y.T. Fong, S.P. Ju, X.H. Du, H.J. Pei, and T.G. Nieh. Assessing the interfacial strength of an amorphous-crystalline interface. *Acta Materialia*, 61(9):3304–3313, 2013.

[18] V. Kokotin, H. Hermann, and J. Eckert. Computer simulation of the matrix-inclusion interphase in bulk metallic glass based nanocomposites. *Journal of Physics:Condensed Mattter*, 23:425403, 2011.

[19] Yinmin Wang, Ju Li, Alex V. Hamza, and Troy W. Barbee. Ductile crystalline-amorphous nanolaminates. *Proceedings of the National Academy of Sciences*, 104(27):11155–11160, 2007.

[20] C. Brandl, T.C. Germann, and A. Misra. Structure and shear deformation of metallic crystalline-amorphous interfaces. *Acta Materialia*, 61(10):3600 – 3611, 2013.

[21] F. C. Frank and J. S. Kasper. Complex alloy structures regarded as sphere packings. I. definitions

and basic principles. *Acta Crystallogr.*, 11:184–190, 1958.

[22] Chris H. Rycroft, Gary S. Grest, James W. Landry, and Martin Z. Bazant. Analysis of granular flow in a pebble-bed nuclear reactor. *Phys. Rev. E*, 74:021306, 2006.

[23] Chris H. Rycroft. Voro++: A three-dimensional Voronoi cell library in C++. *Chaos*, 19:041111, 2009.

[24] Cang Fan, R. T. Ott, and T. C. Hufnagel. Metallic glass matrix composite with precipitated ductile reinforcement. *Applied Physics Letters*, 81(6):1020–1022, 2002.

[25] Wei Hua Wang, D. W. He, D. Q. Zhao, Y. S. Yao, and M. He. Nanocrystallization of ZrTiCuNiBeC bulk metallic glass under high pressure. *Appl. Phys. Lett.*, 75:2770–2772, 1999.

[26] Q. P. Cao, J. F. Li, and Y. H. Zhou. Effect of rolling deformation on the microstructure of bulk $Cu_{60}Zr_{20}Ti_{20}$ metallic glass and its crystallization. *Acta Materialia*, 54:4373–4383, 2006.

[27] T. J. Kulik. Nanocrystallization of metallic glasses. *Journal of Non-Crystalline Solids*, 287:145–161, 2001.

[28] M. S. Daw and M. I. Baskes. Embedded-atom method: Derivation and application to impurities, surfaces, and other defects in metals. *Phys. Rev. B*, 29:6443, 1984.

[29] Y. Q. Cheng, E. Ma, and H. W. Sheng. Atomic level structure in multicomponent bulk metallic glass. *Phys. Rev. Lett.*, 102:245501, 2009.

[30] Y. Q. Cheng, E. Ma, and H. W. Sheng. Alloying strongly influences the structure, dynamics, and glass forming ability of metallic supercooled liquids. *Applied Physics Letters*, 93(11):111913, 2008.

[31] Large-scale Atomic/Molecular Massively Parallel Simulator, LAMMPS, available at: http://lammps.sandia.gov.

[32] S. J. Plimpton. Fast parallel algorithms for short-range molecular dynamics. *J. Comp. Phys.*, 117:1–19, 1995.

[33] Burkhard Dünweg and Wolfgang Paul. Brownian dynamics simulations without gaussian random numbers. *International Journal of Modern Physics C*, 2(3):817–827, 1991.

[34] T. Schneider and E. Stoll. Molecular-dynamics study of a three-dimensional one-component model for distortive phase transitions. *Phys. Rev. B*, 17(3):1302–1322, 1978.

[35] H. J. Berendsen, J. P. M. Postma, W. F. van Gunsteren, A. Di Nola, and J. R. Haak. Molecular dynamics with coupling to an external bath. *J. Chem. Phys.*, 81:3684–3690, 1984.

[36] Seok-Woo Lee, Moo-Young Huh, Eric Fleury, and Jae-Chul Lee. Crystallization-induced plasticity of Cu-Zr containing bulk amorphous alloys. *Acta Materialia*, 54(2):349 – 355, 2006.

[37] B.F. Lu, J.F. Li, L.T. Kong, and Y.H. Zhou. Correlation between mechanical behavior and glass forming ability of Zr-Cu metallic glasses. *Intermetallics*, 19(7):1032 – 1035, 2011.

[38] B.F. Lu. *Structure, glass forming ability and mechanical properties of Cu-Zr-M metallic glasses.* Ph. D dissertation, Shanghai Jiao Tong University, Shanghai, 2013.

[39] John J. Rehr, Joshua J. Kas, Fernando D. Vila, Micah P. Prange, and Kevin Jorissen. Parameter-free calculations of X-ray spectra with FEFF9. *Phys. Chem. Chem. Phys.*, 12(21):5503–5513, 2010.

[40] Paul J. Steinhardt, David R. Nelson, and Marco Ronchetti. Bond-orientational order in liquids and glasses. *Phys. Rev. B*, 28:784–805, 1983.

[41] A. C. Finnefrock, K. L. Ringland, J. D. Brock, L. J. Buller, and H. D. Abruña. Nucleation and ordering of an electrodeposited two-dimensional crystal: Real-time X-ray scattering and electronic measurements. *Phys. Rev. Lett.*, 81:3459–3462, 1998.

[42] Ruslan L. Davidchack and Brian B. Laird. Direct calculation of the hard-sphere crystal /melt interfacial free energy. *Phys. Rev. Lett.*, 85:4751–4754, 2000.

[43] J. J. Hoyt, Mark Asta, and Alain Karma. Method for computing the anisotropy of the solid-liquid interfacial free energy. *Phys. Rev. Lett.*, 86:5530–5533, 2001.

[44] W. Kabsch. A solution for the best rotation to relate two sets of vectors. *Acta Crystallographica Section A*, 32(5):922–923, 1976.

[45] Y.Q. Cheng and E. Ma. Atomic-level structure and structure-property relationship in metallic

glasses. *Progress in Materials Science*, 56:379–473, 2011.

[46] Jun Ding, Yong-Qiang Cheng, and Evan Ma. Full icosahedra dominate local order in $Cu_{64}Zr_{34}$ metallic glass and supercooled liquid. *Acta Materialia*, 69(0):343 – 354, 2014.

[47] M. Alcoutlabi and G. B. McKenna. Effects of confinement on material behaviour at the nanometre size scale. *J. Phys.: Condens. Matt.*, 17:R461–R524, 2005.

[48] J. Q. Broughton and G. H. Gilmer. Molecular dynamics of the crystal-liquid interface. V. structure and dynamics of crystal-melt systems. *The Journal of Chemical Physics*, 84(10):5749–5758, 1986.

[49] J. Pablo Palafox-Hernandez, Brian B. Laird, and Mark Asta. Atomistic characterization of the Cu-Pb solid-liquid interface. *Acta Materialia*, 59(8):3137–3144, 2011.

[50] Yang Yang, David L. Olmsted, Mark Asta, and Brian B. Laird. Atomistic characterization of the chemically heterogeneous Al-Pb solid-liquid interface. *Acta Materialia*, 60(12):4960–4971, 2012.

[51] A. Kerrache, J. Horbach, and K. Binder. Molecular-dynamics computer simulation of crystal growth and melting in $Al_{50}N_{50}$. *EPL (Europhysics Letters)*, 81(5):58001, 2008.

[52] G.Q. Yang, J.F. Li, Q.W. Shi, and L.T. Kong. Structural and dynamical properties of heterogeneous solid-liquid Ta-Cu interfaces: A molecular dynamics study. *Computational Materials Science*, 86(0):64 – 72, 2014.

[53] James M. Howe. Direct observation of order in the liquid at a solid-liquid interface by high-resolution transmission electron microscopy. *Philosophical Magazine A*, 74(3):761–775, 1996.

[54] Adham Hashibon, Joan Adler, Michael W. Finnis, and Wayne D. Kaplan. Atomistic study of structural correlations at a liquid-solid interface. *Computational Materials Science*, 24(4):443 – 452, 2002.

[55] M.Z. Li, C.Z. Wang, S.G. Hao, M.J. Kramer, and K.M. Ho. Structural heterogeneity and medium-range order in Zr_xCu_{100-x} metallic glasses. *Physical Review B*, 80:184201, 2009.

[56] S. Izumi, S. Hara, T. Kumagai, and S. Sakai. Structural and mechanical properties of well-relaxed amorphous-crystal interface in silicon: molecular dynamics study. *Computational Materials Science*, 31:279–286, 2004.

[57] Ling Ti Kong and Laurent J. Lewis. Structure and energetics of c-Si/a-SiO_2 system: Planar interfaces and embedded Si nanocrystals. *Physical Review B*, 77:085204, 2008.

[58] R.L. Davidchack and B.B. Laird. Direct calculation of the crystal-melt interfacial free energies for continuous potentials: Application to the Lennard-Jones system. *Journal of Chemical Physics*, 118(16):7651–7657, 2003.

[59] Lianjun Huang, Jianqiu Zhou, Shu Zhang, Ying Wang, and Yingguang Liu. Effects of interface and microstructure on the mechanical behaviors of crystalline cu-amorphous Cu/Zr nanolaminates. *Materials and Design*, 36:6–12, 2012.

[60] D. Turnbull. Formation of crystal nuclei in liquid metals. *Journal of Applied Physics*, 21(10):1022–1028, 1950.

[61] D. Y. Sun, M. Asta, J. J. Hoyt, M. I. Mendelev, and D. J. Srolovitz. Crystal-melt interfacial free energies in metals: fcc versus bcc. *Physical Review B*, 69:020102, 2004.

[62] J. J. Hoyt, M. Asta, and D. Y. Sun. Molecular dynamics simulations of the crystal-melt interfacial free energy and mobility in Mo and V. *Philosophical Magazine*, 86(24):3651–3664, 2006.

[63] D. Y. Sun, M. Asta, and J. J. Hoyt. Crystal-melt interfacial free energies and mobilities in fcc and bcc Fe. *Phys. Rev. B*, 69:174103, 2004.

[64] Agathagelos Kyrlidis and Robert A. Brown. Density-functional theory and atomistic simulation of the hard-sphere melt-solid interface. *Phys. Rev. E*, 51:5832–5845, Jun 1995.

[65] Kirit Lad, Mohammed Maaroof, K. G. Raval, and Arun Pratap. Fractal growth kinetis during crystallization of amorphous $Cu_{50}Zr_{50}$. *Progress in Crystal Growth and Characterization of Materials*, 45:15–19, 2002.

[66] Yunfeng Shi and Michael L. Falk. A computational analysis of the deformation mechanisms of a nanocrystal-metallic glass composite. *Acta Materialia*, 56:995–1000, 2008.